RSC Advances

PAPER

View Article Online
View Journal | View Issue

Cite this: *RSC Adv.*, 2025, **15**, 289

Laser-induced graphene functionalized cationic porphyrin: fabrication, characterization, and intra-supramolecular electron transfer process†

Karim Mousa,[a] Ahmed Abd El-Moneim,[a] Samir F. El-Mashtoly,[b]
Mohamed Mokhtar Mohamed[c] and Mohamed E. El-Khouly*[a]

Received 6th August 2024
Accepted 6th December 2024

DOI: 10.1039/d4ra05710d

rsc.li/rsc-advances

We report herein a facile synthesis, characterization, and the electron transfer reaction of a novel light-harvesting material composed of laser-induced graphene (LIG) functionalized with the photoactive 5,10,15,20-tetrakis(4-trimethylammoniophenyl)porphyrin tetra(*p*-toluenesulfonate) dye (TTMAPP). LIG was easily fabricated on the surface of a polyimide sheet using VersaLASER 3.6 (VLS 3.6 DT), this method has the advantages of being a simple one-step process and eliminating the impacts of solvents, high-temperature, *etc.* The structural and morphological characterization of the LIG@TTMAPP composite was investigated using various techniques. The steady-state absorption studies showed clearly the successful self-assembly of the TTMAPP dye over the surface of LIG forming the stable LIG@TTMAPP composite. The fluorescence studies showed the occurrence of the intramolecular electron transfer reaction from TTMAPP to LIG. Based on fluorescence lifetime measurements, the rate and efficiency of the electron transfer were determined to be 1.32 × 10^9 s^{-1} and 95%, respectively. The findings that the examined LIG@TTMAPP composite exhibited a facile synthesis, absorbing the light in a wide range of the solar spectrum, with good stability, fast and efficient electron transfer process in an aqueous solution render it as a potential candidate for optical and optoelectronic applications.

Introduction

The current global energy and environmental crisis has led to significant declines in energy resources, environmental degradation, and economic challenges due to the world's rapidly increasing energy consumption. Urgent international action is necessary to advocate for the development of sustainable and renewable energy sources. To pursue such a strategy, the global community must work toward the creation of energy solutions that are accessible, cost-effective, environmentally friendly, and economically viable.[1–6] Among these, solar energy stands out as a highly promising solution.[7–9] However, the efficiency of solar conversion systems remains a significant challenge.

Advanced materials like graphene and its derivatives are emerging as critical components in the next generation of solar conversion systems due to their exceptional conductivity, tunable electronic properties, and ability to facilitate efficient charge separation and transport.[10,11] Among the various derivatives of graphene materials, the synthesized laser-induced graphene (LIG), a three-dimensional porous graphene material with interconnected flakes composed of five, six, or seven atoms and a thickness of approximately 20 microns, attracted much attention in recent years. Along this line, Tour *et al.* transformed commercial polyimide into 3D porous graphene in the air in 2014 using direct laser writing (DLW) technology.[12] This fabrication method involves a one-step process that avoids the need for solvents, high-temperature conditions, or additional treatments. The LIG exhibits promising characteristics for enhancing solar conversion systems, including a porous, conductive structure with a large surface area, rendering it well-suited for functionalization with light-absorbing molecules.[13]

Porphyrin derivatives, on the other hand, are known to be very efficient photoactive substances, which makes them ideal for integration into solar energy conversion systems. Their promise is fueled by their remarkable chemical and photochemical stability, a broad π-conjugated system that allows for strong absorption across the visible spectrum, and versatile reactivity, which includes the ability to modify ring structures and insert a variety of metal ions into the central cavity. Additionally, they are useful for improving photoinduced charge separation processes due to their redox-active nature and capacity for electron transfer reactions.[14–17]

---

[a] Nanoscience Program, Institute of Basic and Applied Sciences, Egypt-Japan University of Science and Technology, New Borg El-Arab City, Alexandria, Egypt. E-mail: mohamed.elkhouly@ejust.edu.eg

[b] Leibniz Institute of Photonic Technology, Albert-Einstein-Straße 9, Jena 07745, Germany

[c] Department of Chemistry, Faculty of Science, Benha University, Benha, Egypt

† Electronic supplementary information (ESI) available. See DOI: **https://doi.org/10.1039/d4ra05710d**

Taking it into consideration, we examine herein the self-assembly of the fabricated laser-induced graphene (LIG) with the photoactive cationic porphyrin dye, namely 5,10,15,20-tetrakis(4-trimethylammoniophenyl)porphyrin tetra(*p*-toluenesulfonate) (TTMAPP), in an aqueous medium (Fig. 1). The structural, morphological, and optical studies of the fabricated LIG@TTMAPP composite have been examined using various spectroscopic techniques. The functionalization of laser-induced graphene using cationic porphyrins would be expected to improve the efficiency of light energy conversion. This enhancement is achieved by promoting rapid electron transfer and reducing charge recombination, both of which are essential for optimizing the device's overall performance. To our knowledge, self-assembled LIG–cationic porphyrin composite in water is rare in the literature.

Experimental section

Chemicals and materials

5,10,15,20-Tetrakis(4-trimethylammoniophenyl)porphyrin tetra(*p*-toluenesulfonate) (TTMAPP) was purchased from Sigma-Aldrich, purity 88% (HPLC) and 90% dye content. A commercial PI film (Kapton) with a thickness of 125 microns was purchased from McMaster-Carr (Cat. No. 2271K6).

Preparation and characterization techniques

LIG design was formulated by coral drawing a 1 cm × 1 cm square shape. Laser processing was performed on a universal laser engraving-cutting machine (3.6 DT), equipped with a 50 W maximum power laser CO_2 source producing a 10.6 μm wavelength. The laser was automated to work at 1000 pulses per inch. To confirm the prepared composites' crystallographic structures, XRD (Shimadzu-X-Lab 600, Japan) was carried out at 40 kV with Cu Kα radiation. The information on functional groups of the prepared materials was determined using Attenuated Total Reflection Fourier Transform Infrared ATR-FTIR by BRUKER INVENIO S. The infrared spectrometer (Bruker Alpha Platinum, Germany) with an internal reflection element (diamond) with a resolution of 4 cm^{-1} and a sweep of 32 scans in the mid-infrared range (4000–500 cm^{-1}) was utilized. An alpha300 RA confocal Raman microscope (WITec, Ulm, Germany) was used to measure the Raman spectra. The Raman excitation source is a frequency-doubled Nd:YAG laser operating at 532 nm (Crystal Laser, Reno, NV, USA). Using a single-mode optical fiber, the laser beam is connected to the microscope. It is collimated and focused on the sample using an Olympus, Japan, 100×/NA 0.90 objective. The surface chemistry, elemental composition, and bonding status were further investigated using K-Alpha X-ray Photoelectron

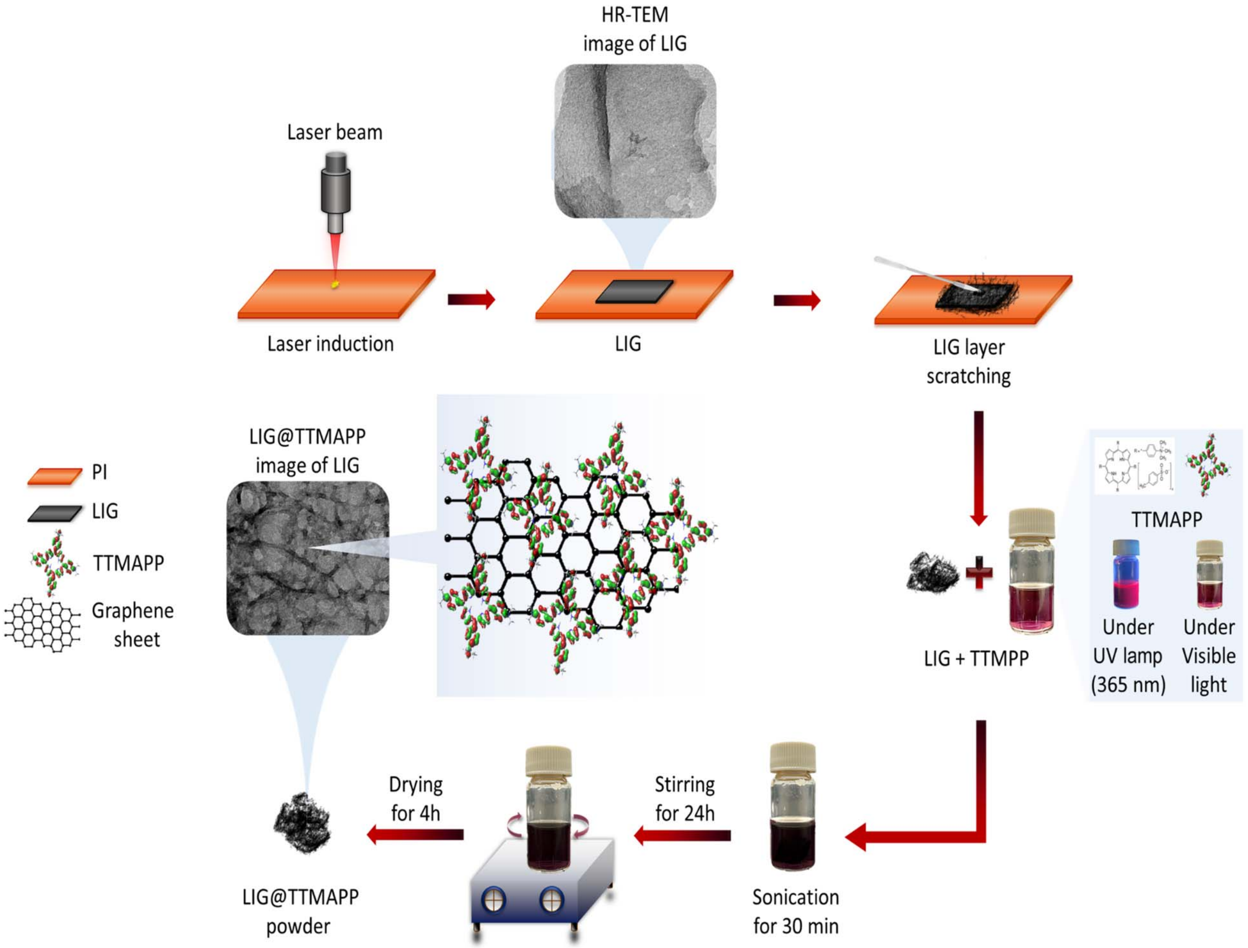

Fig. 1 The schematic diagram for the fabrication of the light-harvesting LIG@TTMAPP composite.

Spectroscopy (XPS) Thermo Fisher Scientific-US. A zeta potential analyzer from Malvern Nano_ZS Instruments was used to investigate the surface charge. The morphologies of the fabricated composite were examined using the high-resolution transmission electron microscopy (HR-TEM) technique at 200 kV. The *d*-spacing was measured using Gatan digital micrograph software. TEM model JEOL JEM-2100F, Japan. The specimens' average surface roughness (R_a) was determined using a 3D laser scanning microscope (Keyence VK-X100, Keyence GmbH, Neu-Isenburg, Germany). All measurements are taken at 20× magnification using a laser light microscope. The wavelength of the laser was 658 nm. The specimens were placed on the platform, and three distinct areas were measured on each specimen. The measured area was 705 × 705 μm. The scan speed was 102 $\mu m\ s^{-1}$. Steady-state absorption and fluorescence spectra were recorded using a UV-vis spectrophotometer (Shimadzu UV-2600) and spectrofluorometer (Shimadzu RF-6000), respectively. To determine the electron-transfer rate of the LIG@TTMAPP supramolecular carbon nanostructure the picosecond fluorescence decay profiles were measured by the single photon counting technique using Fluor Hub (Horiba Scientific). Lifetime was evaluated with the software Decay Analysis 64 by Horiba Scientific attached to the equipment.

Fabrication of LIG using VLS 3.6 DT

The VLS 3.6 laser system provides a range of adjustable parameters that allow for the implementation of various effects during the printing procedure. The engraving patterns were designed utilizing Corel Draw software, resulting in a square-shaped design measuring 1 cm × 1 cm, as depicted in Fig. S1.† This design was subsequently transferred to the VLS 3.6 DT printing machine software for execution. The synthesis parameters were optimized in the software to yield the highest flexibility and conductivity: a laser power of 3.6 watts, a laser speed of 3.5 inches per second, and 1000 pulses per inch. The polyamide was positioned at the focal point of the laser source by adjusting the *Z*-axis to ensure maximum burning. After adhering the film to a glass piece, it was placed within the laser compartment platform. Meticulous care was taken to maintain a clean Kapton surface by washing it with ethanol and preventing air pockets beneath the film during the mounting process. Lastly, the LIG film was scratched from the polyimide surface, and dissolved in 3.5 ml of distilled water.

Fabrication of the LIG@TTMAPP

1.5 mg of 5,10,15,20-tetrakis(4-trimethylammoniophenyl) porphyrin tetra(*p*-toluenesulfonate), (TTMAPP) was dissolved in 3.5 ml of distilled water. The solution was then subjected to sonication for 30 minutes to ensure homogeneity, after which it underwent self-assembly onto the previously prepared LIG solution. Subsequently, the composite solution was stirred for 24 hours and then dried for 4 hours in a drying oven.

Results and discussions

Structural characterization of LIG and the LIG@TTMAP

Fig. 2A exhibited the X-ray diffraction pattern (XRD) of LIG, TTMAPP, and LIG@TTMAPP composite. LIG exhibits a broad diffraction peak from 17.23° to 37° even though we could observe a distinct peak at $2\theta = 25.54°$ with an interplanar distance (I_c) of 0.34 nm, which can be indexed to the distance between the (002) in the LIG.[12,18] The broadening in the diffraction peak can be assigned to the porous structure of LIG,[12,18] also could be attributed to defects on the graphene hexagonal layers, as well as the presence of oxygen functional groups and nitrogen groups with the carbon moieties. The recorded peaks at $2\theta = 44.18°$ can be indexed to (100) reflections with an interplanar distance of 0.20 nm.[19,20] This peak is associated with the reduction of the precursor material into the graphene-like LIG structure. It is related to the in-plane features of the laser-induced graphene and reflects the planar arrangement of the material. The laser-induced graphitization process may be driven by the presence of recurring aromatic and amide functionalities within the precursor polymer. On the other hand, the XRD data shown of the LIG@TTMAPP composite, the peak of the (002) has transferred to $2\theta = 26.3°$ corresponds to an interplanar distance of 0.33 nm. Also, the peak at the (100) plane shifted from $2\theta = 44.18°$ to $2\theta = 43.22°$ which corresponds to (100) and has an interplanar distance d of 0.21 nm,[21,22] the decrease in the interplanar distance of the (002) peak could be attributed to the insertion of TTMAPP in the porous structure of LIG forming higher stress on the hexagonal planar sheets. Also, the increase in the interplanar distance of the (100) peak could be formed due to the electrostatic repulsion between the sulphonate group in the porphyrin and the negative graphene sheet.[12,23]

To examine the surface chemistry and bonding status structures of the LIG and LIG@TTMAPP, XPS test was performed as shown in Fig. 2B. The XPS survey of LIG and LIG@TTMAPP comparison shows the XPS survey of LIG, three elements can be detected, carbon (C 1s), oxygen (O 1s) and nitrogen (N 1s) with 90.55%, 8.89% and 0.56% atomic percentage, respectively. The deconvolution of the carbon (C 1s) is shown in Fig. S2.† The recorded peak at 284.2 eV can be assigned to the sp^2 (C–C/C=C) carbon bonding which arises from the primary graphitic structure of LIG.[24] The recorded peak appears at 285.1 eV could be assigned to sp^3 (C–C) carbon bonding indicating the presence of structural defects from the laser scribing process.[25] The peak at 289.61 eV could be assigned to the carbonyl group (–C=O/–COOH) which arises from the laser scribing process of polyimide.[26] The most dominant bonding structure in LIG is the sp^2. The deconvolution of (O 1s) shown in Fig. S2† exhibited a maximum peak of 532.41 eV that can assigned to the surface hydroxyl group (OH).[27] Nitrogen (N 1s) deconvolution which has two peaks; 399.7 eV can be assigned to pyrrolic nitrogen,[28] 405.7 eV may be attributed to either the presence of amino groups including those in saturated heterocyclic amines, or the existence of pyridinic oxide functional groups.[28]

On the other hand, the LIG@TTMAPP survey shown in Fig. 2B showed the presence of six elements, carbon (C 1s), oxygen (O 1s), nitrogen (N 1s), sulfur (S 2p), ferric (Fe 2p) and calcium (Ca 2p) with 74.6%, 16.39%, 6.93%, 0.16%, 1.27% and 0.66% atomic percentage, respectively. The deconvolution of the carbon (C 1s) shown in Fig. S3† exhibited three peaks at

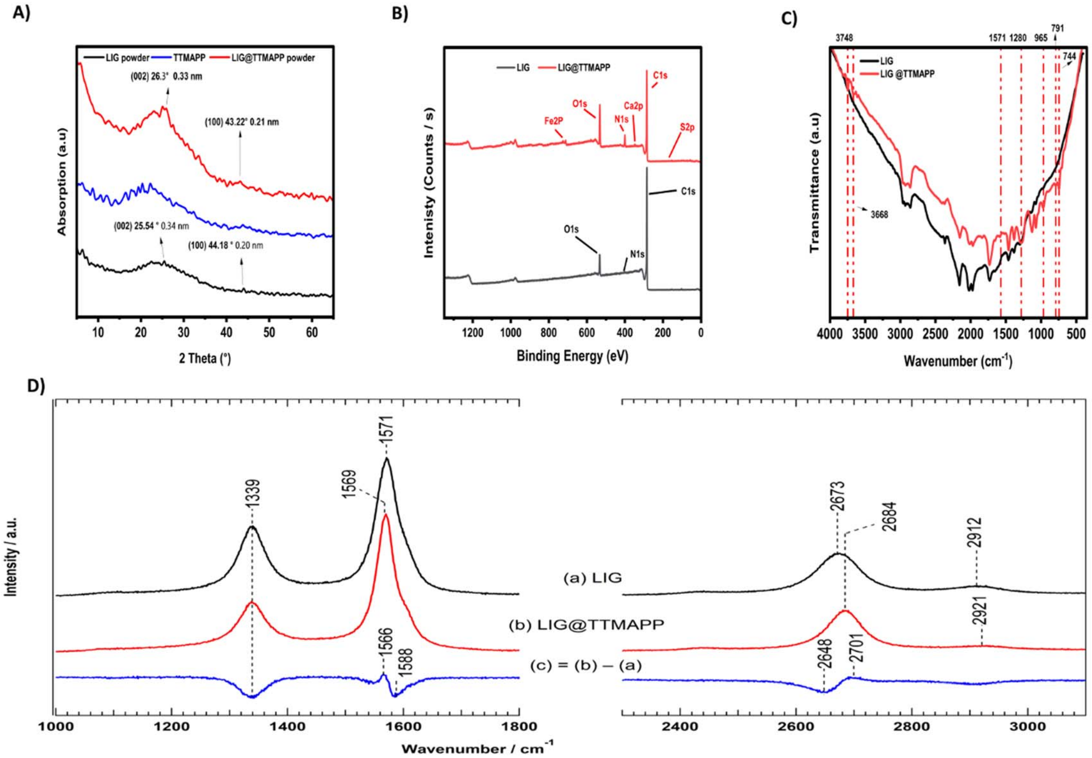

Fig. 2 (A) X-ray diffraction patterns of LIG powdered scraped from polyimide, TTMAPP, and LIG@TTMAPP composite. (B) XPS survey for LIG and LIG@TTMAPP. (C) FTIR curves of LIG, and LIG@TTMAPP composite from 500 to 4000 cm^{-1}. (D) Raman spectra for LIG, and LIG@TTMAPP composite.

284.36, 285.45, and 288.08 eV that could assigned to sp^2 (C–C/C═C) carbon bonding,[24] sp^3 carbon bonding,[25,29] and (O–C═O),[25] respectively. The deconvolution of oxygen (O 1s) shown in Fig. S3† shows a peak at 531.64, which can be attributed to the carbonyl groups (C═O).[24] The deconvolution of nitrogen (N 1s) shows peaks at 399.85 and 402.69 eV that are assigned to pyrrolic nitrogen[28] and quaternary nitrogen,[30] respectively, indicating the successful functionalization of graphene sheets with the porphyrin moiety. The deconvolution of sulfur (S 2p) shown in Fig. S3† shows the presence of two peaks 168.07 and 171.92 eV which can be assigned to sulphones[31] and bisulfate HSO_4 complexes, respectively.[32] In general, the increment in the percentages of oxygen nitrogen, and sulfur that exist in the TTMAPP structure proves the successful functionalization of TTMAPP on the surface of LIG. It should be noted that the presence of both calcium and iron ions could be attributed to the commercial-grade dye of TTMAPP and/or the presence of ferric traces in the commercial polyimide.[20]

To examine the functional groups, the FT-IR spectra of polyimide, LIG, TTMAPP, and LIG@TTMAPP composite were performed. As seen from Fig. S4,† the peaks in the range of 600 to 4000 cm^{-1} were assigned to the polyimide. The peak at 719 cm^{-1} can be assigned to the imide ring deformation vibrations, particularly the out-of-plane bending of the C═O and C–N–C groups in the imide structure. The peak at 816 cm^{-1} was assigned to the out-of-plane bending vibrations of aromatic C–H bonds. The recorded bands at 1087, 1116, 1167, 1235, 1364, and 1498 cm^{-1} are mainly associated with C–O–C stretching (ether linkage) and in-plane aromatic C–H bending, the symmetric stretching vibrations of the C–O–C bond in the ether linkage, the asymmetric C–O–C stretching (ether linkage) and possibly some C–N stretching vibrations within the imide ring, the asymmetric stretching of the C–N bond in the imide group and C–O–C stretching within the ether linkage, the stretching vibration of the imide C–N, and the stretching vibrations of the aromatic C═C bonds in the benzene rings, respectively. Finally, the bands at 1710 and 1776 cm^{-1} are assigned to asymmetric and symmetric stretching vibrations of the imide carbonyl groups.[33,34]

On the other hand, the laser scribing of LIG exhibits different features as shown in Fig. 2C. A broad absorption peak in the region between 2997 and 2852 cm^{-1} was assigned to the sp^2/sp^3 stretching vibration of the C–H bonds.[24,35] The recorded peak at 2164 cm^{-1} was assigned to C≡C stretching vibrations.[36] The peak recorded at 2029 cm^{-1} was assigned to ketenimine CH_2CNH.[37] The peak around 1730 cm^{-1} can be assigned to carbonyl and carboxyl groups (C═O).[38] The peak around 1632 cm^{-1} can be assigned to sp^2 carbon (C═C) stretch.[38] The spectrum exhibited a weak peak at 1450 cm^{-1} that can be ascribed to the deformation vibration of the methyl functional group ($-CH_3$), while the weak peak at 1364 cm^{-1} corresponds to the symmetric and asymmetric deformation modes of the C–H covalent bonds.[39] The peaks around 1126 and 1071 cm^{-1} can be assigned to the epoxide groups (C–O–C), and epoxy groups (C–

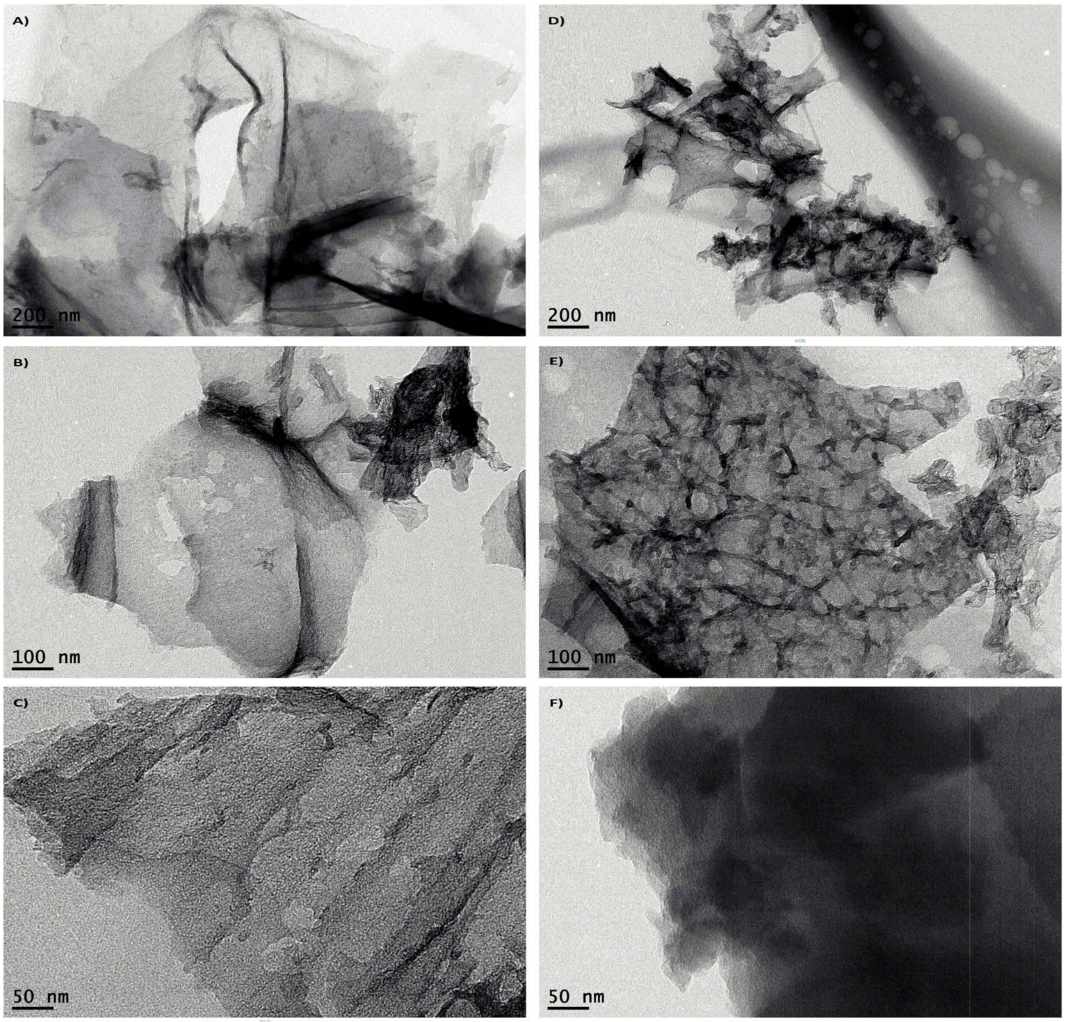

Fig. 3 HRTEM image of (A–C) LIG, and (D–F) LIG@TTMAPP composite with the same magnifications. The high-intensity black areas represent the loaded TTMAPP composite porphyrin molecules over the surface of LIG.

O).[38] A broad line from 1000 to 500 cm^{-1} shows the laser scribing effect.[13,38]

Fig. S4† exhibited the porphyrin-free base's typical vibrations, where TTMAPP dye exhibited vibrational peaks at 3438 and 1000 cm^{-1} that agree with the N–H stretching and C–N stretching and bending vibrations, respectively. Furthermore, the recorded peak at nearly 815 cm^{-1} was associated with the macrocycle ring's out-of-plane deformation. When turning into the FTIR spectra of the LIG@TTMAPP composite, it is clear that the spectra exhibited 7 new peaks, the 3747 cm^{-1} band is most likely assigned to the (–CONH–) unit.[40] The peak at 3668 cm^{-1} could be assigned to (OH) stretching.[41] The peak around 1571 cm^{-1} could be assigned to C═N stretching.[42] The peak at 1281 cm^{-1} could be assigned to carbonyl (–C–O) wagged vibration,[43] The peak around 1571 cm^{-1} could be assigned to C═N stretching.[44] The peak at 1281 cm^{-1} could be assigned to carbonyl (–C–O) wagged vibration,[41] 965 cm^{-1} band was assigned to C═C bending alkene, 791 cm^{-1} band was assigned to C–H bending of 1,2,3,4-tetra substituted, 744 cm^{-1} band that assigned to C–H bending 1,2-disubstituted. Based on the recorded peaks shown above, one can suggest the successful formation of LIG@TTMAPP composite through the electrostatic interactions.[42,45]

Raman spectroscopy is an advanced analytical method utilizing the inelastic scattering of monochromatic light. It can deliver precise insights into molecular vibrations, chemical compositions, and crystal structures making it highly versatile.[46–48] The laser-induced portions were examined using Raman spectroscopy to further characterize the structural alteration of the LIG and LIG@TTMAPP samples, as illustrated in Fig. 2D. LIG exhibits four distinct peaks of graphitic carbon: a D peak at 1339 cm^{-1}, D′ peak at 1608 cm^{-1}, which arises due to defects or disorders in the graphene lattice, such as vacancies, edges, and structural imperfections in sp^2 hexagonal carbon structures,[49,50] a G peak at 1571 cm^{-1} that arises due to structures derived from carbon atoms, and a 2D peak at 2673 cm^{-1} arises from second-order Raman scattering by boundary phonons of the Brillouin zone.[50,51] The LIG has $I_D/I_G = 0.5$ and $I_{2D}/I_G = 0.29$ which represents a multilayer graphene structure with 50 percent deformation in the LIG hexagonal

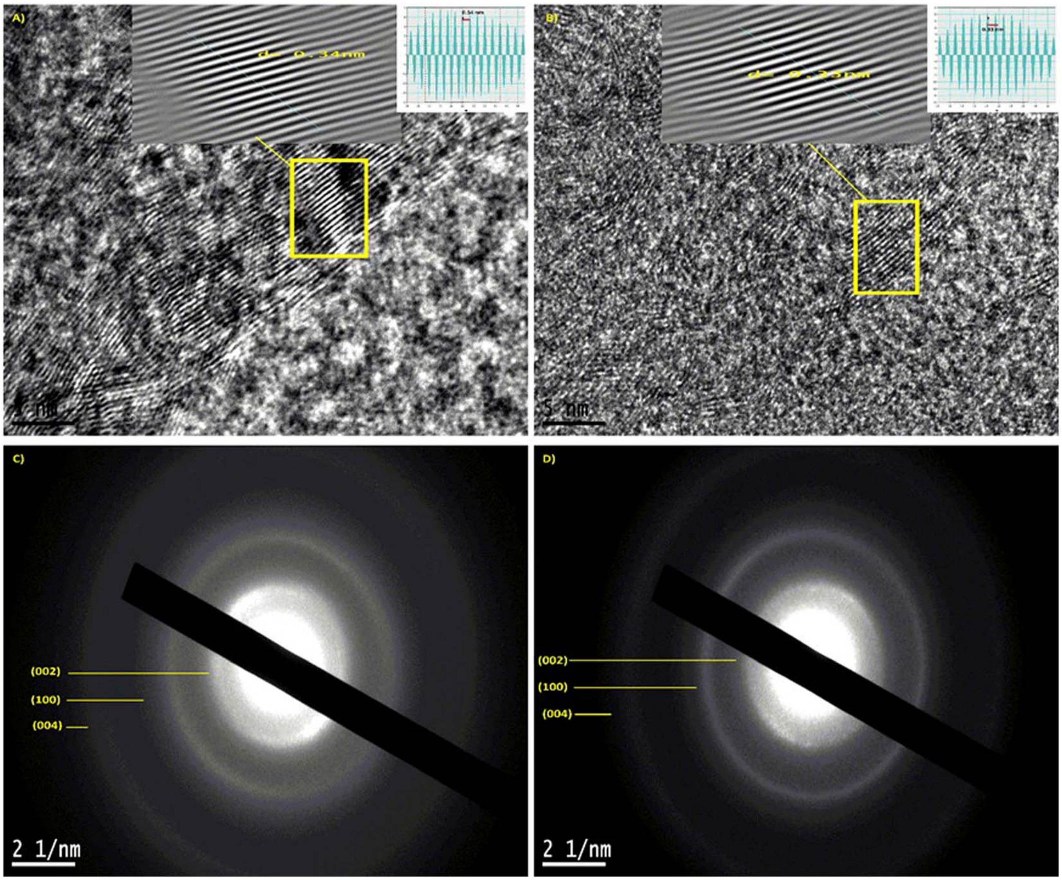

Fig. 4 (A) and (B) 5 nm scale HR-TEM image with the selected area to calculate the interplanar distance, (C) and (D) selected area diffraction pattern to calculate the interplanar distance using HR-TEM.

structure.[52] In multilayer graphene, the 2D band exhibits a broader and less intense profile compared to the G band, while the intensity of the G peak increases as the number of layers rises. This phenomenon is attributed to the increased complexity and interactions occurring between the layers.[53–55]

When turning into LIG@TTMAPP composite shown in spectra (b), one can see peaks at 1339 cm^{-1} D band, D′ 1607 cm^{-1}, 1569 cm^{-1} G band, 2684 cm^{-1} 2D band, $I_D/I_G = 0.35$, $I_{2D}/I_G = 0.29$. As seen, there is no significant change in the carbon structure of graphene, even though there is a noticeable decrement in the defects of the crystalline structure of the LIG. This indeed configures the grafting of TTMAPP onto LIG. Furthermore, spectra (c) displays derivatives at 1566/1588 and 2648/2701 cm^{-1} indicating the wavenumber shift of 1571 and 2673 cm^{-1}, respectively, upon the addition of TTMAPP to LIG. This includes not only a downshift in the wavenumber for the G band by 2 cm^{-1} and an upshift for the 2D band by 11 cm^{-1} but also the decrement in the intensity of the doped-LIG comprehends the potential interaction between porphyrin and LIG. The simultaneous downshift of the G band and upshift of the 2D band upon doping suggests that the TTMAPP is altering both the vibrational properties and the electronic band structure of graphene. This combined effect signifies changes in bond strength, electron density, and electronic interactions within the graphene.[56–58]

The zeta potential analysis conducted on the individual components and the self-assembled LIG@TTMAPP composite provides insights into the charge transfer mechanism. As shown in Fig. S7,† the LIG exhibited a zeta potential of −17.8 mV, indicating a negatively charged surface. TTMAPP dye had a zeta potential of −1.69 mV, reflecting the presence of both cationic nitrate groups and anionic sulfonate groups. The self-assembled LIG@TTMAPP composite displayed a zeta potential of −0.146 mV, suggesting the successful attachment of TTMAPP to LIG. Based on the results obtained from the FTIR, XPS, XRD, and Raman, the attachment of TTMAPP depends on the electrostatic interaction between the nitro group of TTMAPP and the negative charge of graphene sheets.

Morphological characterization

The HR-TEM characterization revealed the formation of a self-assembled structure between TTMAPP and the LIG morphology. The TEM images at various magnifications confirmed the effective deposition of TTMAPP onto the LIG surface, suggesting that the self-assembly likely occurs through the electrostatic interactions between the porphyrin moiety and the porous, defective regions of LIG. As illustrated in Fig. 3A–C, the LIG images display highly illuminated thick layers, indicating the presence of a few graphene layers, while the dense areas correspond to the existence of carboxylic groups and a high density of graphene sheets. In contrast, the LIG@TTMAPP are observed as high-intensity black areas on the LIG sheet, as shown in Fig. 3D–F. To investigate these dense areas, the EDX test was performed. The data of LIG shown in Fig. S5† exhibited 99.5% carbon and 0.5% oxygen, while the LIG@TTMAPP composite exhibited 98.15% carbon and 1.85% oxygen. This finding indicates an increase in the oxygen content due to the incorporation of TTMAPP.

As seen in Fig. 4, the HR-TEM was used to determine the *d*-spacing of LIG and LIG@TTMAPP at 5 nm scale using Gatan digital micrograph software, the (I_c) of the (002) of LIG is 0.34 nm while the (I_c) of LIG@TTMAPP was found to be 0.33 nm.[12] The obtained interplanar distance from the HR-TEM agrees with the results obtained from the XRD. Further, the diffraction pattern obtained for LIG shown in Fig. 4C exhibited three broad diffraction rings which can be indexed to (002), (100), and (004), respectively.[12] On the other hand, LIG@TTMAPP had three diffraction peaks (002), (100), and (004), respectively. The insertion of TTMAPP into the porous structure of LIG appears to have altered the orientation of some planes and decreased the interplanar distance. Additionally, the rings appear slightly sharper, suggesting an increase in the crystallinity of the LIG upon the self-assembly of TTMAPP. The HR-TEM images indicate that the self-assembly of TTMAPP on the graphene sheets results in a new preferred orientation, as demonstrated in the ESI in Fig. S6.† The lattice displays orientations in various directions, with the LIG lattice points exhibiting diverse alignments. After the incorporation of TTMAPP, the lattice structure becomes more organized and exhibits a preferred direction. This indicates that the interaction between LIG and TTMAPP involves the attachment of the cationic porphyrin to the defected sites of LIG, which aligns with the Raman spectra shown in Fig. 2D.

Laser confocal microscope was used to determine the specimens' average surface roughness (R_a), a 3D laser scanning microscope (Keyence VK-X100, Keyence, Neu-Isenburg, Germany) was used. All measurements are performed using a laser light microscope at a 20× magnification (Fig. 5). The laser's wavelength was 658 nm. The specimens were placed on the platform, and each one had three different areas measured. The area that was measured was 705 × 705 μm. The speed of the scan was 102 μm s. For each specimen, the roughness value (μm) was computed by averaging the data acquired from three distinct places. The visual representations of the surfaces were also taken to qualitatively evaluate the surface roughness, in addition to the mathematical means. A color scale and graphics were used to understand the images that were obtained. In the illustrations, each color denotes a distinct value; positive values stand in for peaks and negative values for pits. It was further confirmed that the light-harvesting TTMAPP dye had been loaded onto the surface of LIG. As observed, TTMAPP was successfully loaded over the LIG surface from Fig. 5. The surface roughness values of LIG and the LIG@TTMAPP composite have been determined to be 96.9 and 31.8 μm, respectively. Such a decrease in the surface roughness of the LIG@TTMAPP composite compared to LIG suggests that TTMAPP forms surface treatment to the LIG, taking into consideration that the surface roughness is a crucial metric that further impacts the quality of the self-assembled materials for various optical applications.[59]

Optical studies

The normalized absorption and fluorescence spectra of TTMAPP are illustrated in Fig. 6. The spectra featured a Soret band with a peak wavelength of 412 nm, as well as four weak Q

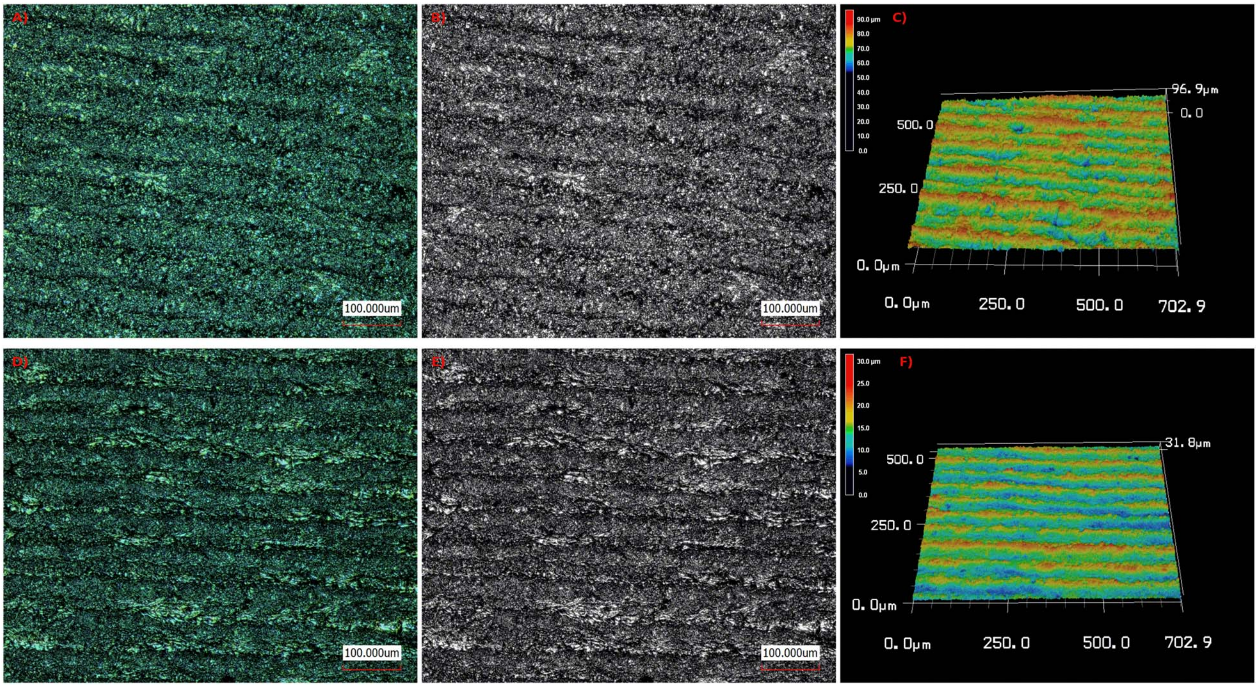

Fig. 5 Laser confocal microscope of (A–C) LIG, and (D–F) the LIG@TTMAPP composite with a 20× magnification.

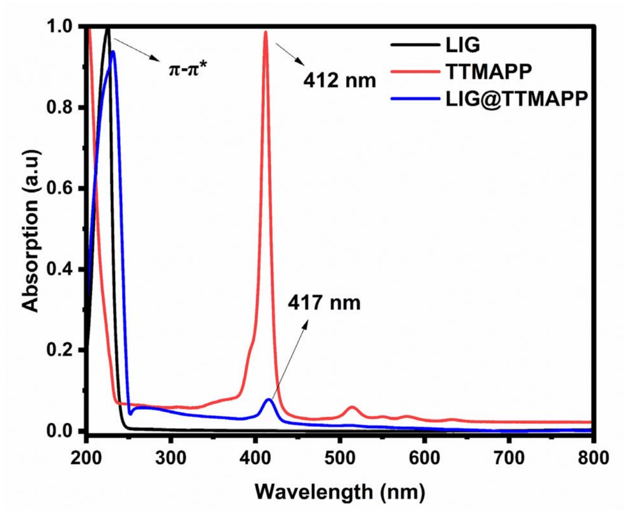

Fig. 6 Normalized absorption spectra of LIG, TTMAPP, and LIG@TTMAPP in water.

vibronic bands at 514, 550, 579, and 633 nm. As seen in Fig. 6, the LIG absorption spectrum displayed a prominent peak at 226 nm, which can be attributed to the π–π* transition of the conjugated aromatic domains within the carbon–carbon framework. The self-assembled LIG@TTMAPP composite exhibited the characteristic peaks of both LIG and TTMAPP, accompanied by a ∼5 nm bathochromic shift in the maximum absorption of TTMAPP when dispersed in water. This spectral shift can be attributed to an increase in the electronic conjugation between the electron-donating TTMAPP moiety and the electron-accepting LIG material.[59]

The fluorescence spectra of TTMAPP and the LIG@TTMAPP composite were subjected to 3D mapping to investigate their isosbestic points. To more thoroughly analyze the changes in fluorescence, a stock solution of TTMAPP was prepared, and the spectrofluorometer was used to irradiate the solution with excitations ranging from 400 nm to 425 nm. The 3D mapping of TTMAPP's excitation *versus* emission, depicted in Fig. 7A and B accompanying figures, confirmed that the maximum fluorescence was observed at 412 nm excitation and 642 nm emission, with isosbestic points appearing at 404 and 416 nm. In contrast, the self-assembly of LIG with TTMAPP shifted the peak of maximum excitation to 413.5 nm, while the maximum fluorescence shifted from 642 to 645 nm. Additionally, the intensity of TTMAPP experienced noticeable quenching upon the addition of LIG. The significant changes in the maximum intensity at different excitations confirm the formation of the LIG@TTMAPP composite, which exhibits a new maximum absorption wavelength, as depicted in Fig. 7C and D.

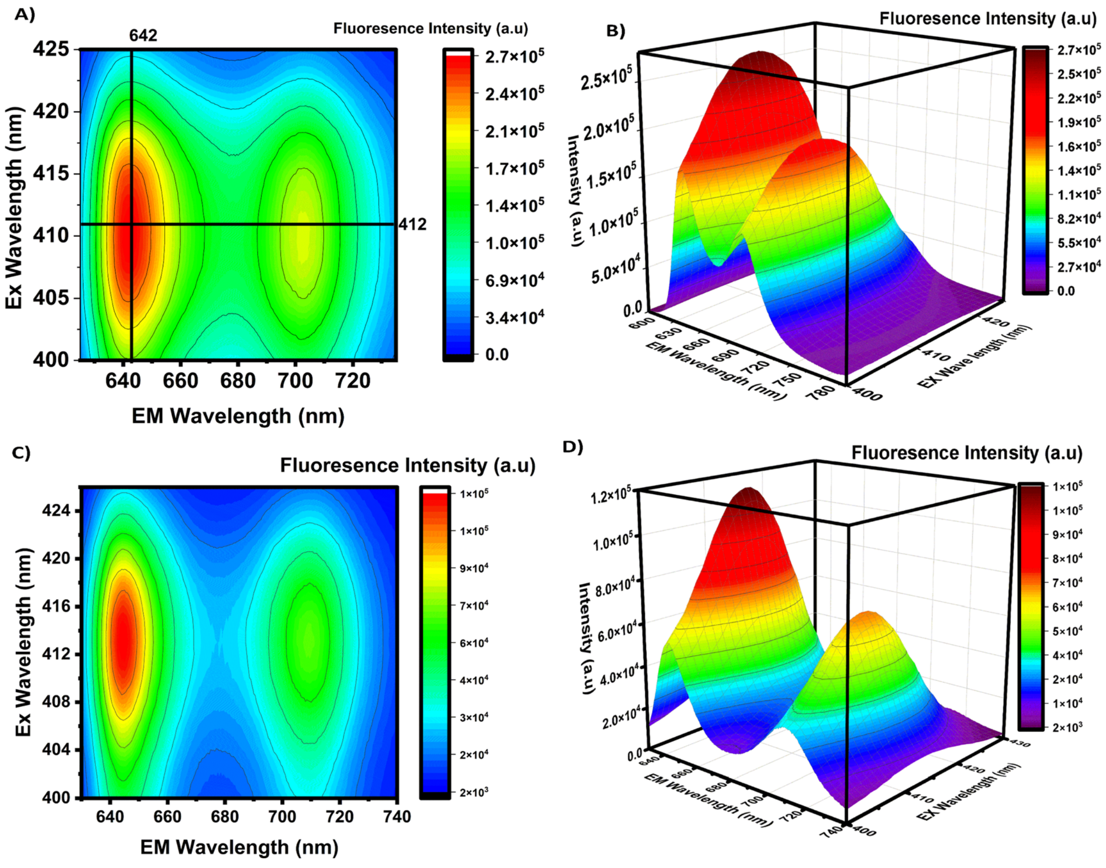

Fig. 7 (A) Plot of the excitation wavelengths (from 400 to 425 nm) *versus* the emission wavelengths of TTMAPP. (B) Map surface of fluorescence of TTMAPP. (C) The plot of the excitation wavelengths (from 400 to 425 nm) *versus* the emission of LIG@TTMAPP composite. (D) 3D map surface of LIG@TTMAPP composite.

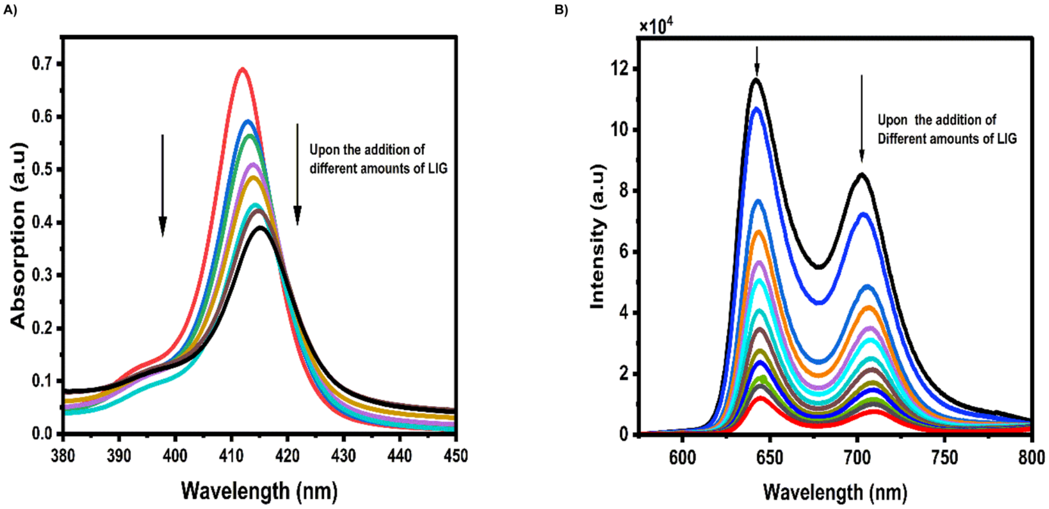

Fig. 8 (A) Absorption spectra of the formation of the self-assembled TTMAPP–LIG in an aqueous medium; (B) emission quenching of TTMAPP by adding various amounts of LIG forming the self-assembled TTMAPP–LIG composite; $\lambda_{ex} = 416$ nm.

Self-assembly for LIG@TTMAPP

The self-assembly process between the two entities resulted in the formation of the LIG@TTMAPP composite, as evidenced by steady-state absorption and fluorescence studies. As depicted in Fig. 8A, the UV-vis absorption spectrum of TTMAPP in water (3.60 μM) exhibited a distinctive Soret band at 412 nm, which is attributed to the ($S_0 \rightarrow S_2$) transition. Upon the addition of varying amounts of LIG to an aqueous TTMAPP solution, the characteristic Soret band of TTMAPP showed a clear decrease in intensity, accompanied by a ~5 nm red shift (towards the longer wavelength). This observation provides clear evidence for the successful incorporation of TTMAPP onto LIG sheets, forming the self-assembled LIG@TTMAPP composite through electrostatic interactions.[59]

Fig. 8B shows the excitation of TTMAPP (3.6 μM) with 416 nm light, as observed from the 3D fluorescence map, generated a fluorescence spectrum in an aqueous solution exhibiting two emission bands at 642 nm (higher ratio) and 702 nm (lower ratio), corresponding to the 0–1 and 0–0 transitions, respectively. Upon the addition of varying quantities of LIG, the fluorescence intensities of the singlet-excited states of TTMAPP were notably quenched, accompanied by a slight red shift of approximately 3 nm. This quenching phenomenon is most likely attributed to intramolecular electron transfer from the electron-donating TTMAPP to the surface of LIG, taking into consideration that the energy transfer process is energetically unfavorable.

Fluorescence lifetime measurements shown in Fig. 9 were used to quantitatively analyze the changes in fluorescence and estimate the kinetics of the electron transfer process within the LIG@TTMAPP composite. Upon photoexcitation of TTMAPP (3.6 μM) with a picosecond pulsed laser (420 ± 10 nm), the fluorescence decay–time profile of the TTMAPP singlet-excited state at 642 nm exhibited a monoexponential decay with a lifetime of 9.56 ns, consistent with previous literature.[60] However, the addition of varying amounts of LIG to an aqueous TTMAPP solution resulted in significant quenching of the fluorescence lifetime. The decay could be satisfactorily fitted to a biexponential function, with a fast decay component followed by a slower decay. The fast-decaying component had a lifetime of 0.70 ns (10%), which is attributed to the electron transfer reaction within the self-assembled composite. The second decay, with a lifetime of 8.72 ns (90%), resembles the decay of the TTMAPP dye. Based on the lifetimes of TTMAPP and the LIG@TTMAPP composite, the rate constant (k_{et}) and quantum yield (k_{et}) of the electron transfer from TTMAPP to LIG were determined to be 1.32×10^9 s^{-1} and 95%, respectively. These findings suggest a fast and efficient intramolecular electron transfer process from the electron-donating TTMAPP to the electron-accepting LIG of the self-assembled LIG@TTMAPP composite.

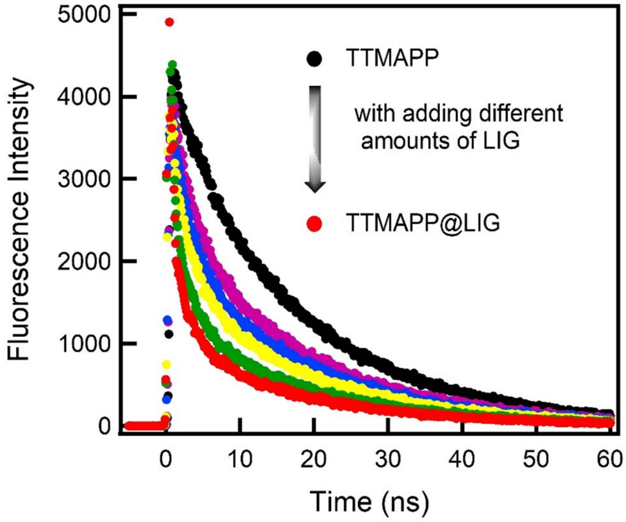

Fig. 9 Fluorescence decay profiles of the singlet TTMAPP (3.6 μM) in the absence and presence of different amounts of LIG in water; $\lambda_{ex} = 420$ nm and $\lambda_{em} = 645$ nm.

Conclusions

We demonstrated herein the synthesis, characterization, and electron transfer reaction of a novel supramolecular LIG@TTMAPP composite in an aqueous medium. The examined material has been constructed by successfully loading the cationic TTMAPP porphyrin dye over the surface of LIG. The crystallographic structure of the system was characterized using X-ray diffraction which showed a decrease in the interplanar distance of LIG. High-resolution transmission electron microscopy showed the TTMAPP loading as high-density black areas on the thick layers of graphene. Accompanied by a sharp diffraction pattern for LIG@TTMAPP which suggests an increase in the crystallinity of the material, also the HR-TEM images confirmed the change in the orientation and the decrease in the interplanar distance. This indicates the stacking and insertion of TTMAPP into the defective and porous sites of LIG. Fourier-transform infrared spectroscopy and XPS and zeta-potential of LIG@TTMAPP confirmed the loading of TTMAPP on the LIG through electrostatic interactions between nitrogen and graphene sheets. Raman spectroscopy showed a significant 15% decrease in the defects of the sp^2 hexagonal carbon structure D-band of LIG@TTMAPP, which agrees well with HR-TEM images. The average surface roughness, measured using a 3D laser scanning microscope, was 96.9 μm for LIG and 31.8 μm for LIG@TTMAPP, indicating an enhancement in the crystallinity of the system as observed in the HR-TEM diffraction pattern and Raman spectroscopy. The steady-state absorption measurements of the LIG@TTMAPP self-assembly showed a significant red shift of approximately 5 nm compared to the control TTMAPP in water. Additionally, the fluorescence intensities of the singlet-excited states of TTMAPP were significantly quenched, accompanied by a ~3 nm red shift, upon adding different amounts of LIG. Based on the time-resolved fluorescence lifetime measurements, the rate and efficiency of the electron transfer were determined to be $1.32 \times 10^9\ s^{-1}$ and 95%, respectively, indicating fast and efficient electron transfer from the singlet-excited state of TTMAPP to the electron-accepting LIG in the self-assembled LIG@TTMAPP composite.

Data availability

Data will be made available on request.

Conflicts of interest

The authors declare no conflict of interest.

Acknowledgements

This paper is based upon work supported by Science, Technology & Innovation Funding Authority (STDF), Egypt, under grant number 46207.

References

1 J. Barber, Photosynthetic energy conversion: natural and artificial, *Chem. Soc. Rev.*, 2009, **38**, 185–196.

2 N. S. Lewis and D. G. Nocera, Powering the planet: chemical challenges in solar energy utilization, *Proc. Natl. Acad. Sci. U. S. A.*, 2006, **103**, 15729–15735.

3 N. S. Lewis, Toward Cost-Effective Solar Energy Use, *Science*, 2007, **315**, 798–801.

4 M. E. El-Khouly, E. El-Mohsnaey and S. Fukuzumi, Solar energy conversion; from natural to artificial photosynthesis, *Science*, 2005, **309**, 548–551.

5 N. Armaroli and V. Balzani, The Future of Energy Supply: Challenges and Opportunities, *Angew. Chem., Int. Ed.*, 2007, **46**, 52–66.

6 I. McConnell, G. Li and G. W. Brudvig, Energy Conversion in Natural and Artificial Photosynthesis, *Chem. Biol.*, 2010, **17**, 434–447.

7 N. Sharma, A. Singh, N. Kumar, A. Tiwari, M. Lal and S. Arya, A review on polyaniline and its composites: from synthesis to properties and progressive applications, *J. Mater. Sci.*, 2024, **59**, 6206–6244.

8 S. Balu, D. Ganapathy, S. Arya, R. Atchudan and A. K. Sundramoorthy, Advanced photocatalytic materials based degradation of micropollutants and their use in hydrogen production – a review, *RSC Adv.*, 2024, **14**, 14392–14424.

9 R. Khajuria, A. Singh, M. D. Rather, A. Sharma, P. Angotra, A. K. Sundramoorthy, S. Dixit, N. I. Vatin and S. Arya, Elucidating the structural, morphological and optical properties of chalcogenide glasses within antimony-tin-selenium ternary system, *Appl. Phys. A: Mater. Sci. Process.*, 2024, **130**, 711.

10 S. G. Jo, R. Ramkumar and J. W. Lee, Recent Advances in Laser-Induced Graphene-Based Materials for Energy Storage and Conversion, *ChemSusChem*, 2023, **17**, e202301146.

11 R. Kumar, R. Pandey, E. Joanni and R. Savu, Laser-induced and catalyst-free formation of graphene materials for energy storage and sensing applications, *Chem. Eng. J.*, 2024, **497**, 154968.

12 J. Lin, Z. Peng, Y. Liu, F. Ruiz-Zepeda, R. Ye, E. L. G. Samuel, M. J. Yacaman, B. I. Yakobson and J. M. Tour, Laser-induced porous graphene films from commercial polymers, *Nat. Commun.*, 2014, **5**, 5714.

13 R. Ye, D. K. James and J. M. Tour, Laser-Induced Graphene: From Discovery to Translation, *Adv. Mater.*, 2018, **31**, 1803621.

14 X. Peng, M. Zhang, H. Qin, J. Han, Y. Xu, W. Li, X. Zhang, W. Zhang, U. Apfel and R. Cao, Switching Electrocatalytic Hydrogen Evolution Pathways through Electronic Tuning of Copper Porphyrins, *Angew. Chem., Int. Ed.*, 2024, **63**, e202401074.

15 D. A. Gkika, K. Ladomenou, M. Bououdina, A. C. Mitropoulos and G. Z. Kyzas, Adsorption and photocatalytic applications of porphyrin-based materials for environmental separation processes: a review, *Sci. Total Environ.*, 2024, **908**, 168293.

16 Y.-C. Feng, X. Wang and D. Wang, Metal porphyrins and metal phthalocyanines as designable molecular model electrocatalysts, *Mater. Chem. Front.*, 2024, **8**, 228–247.

17 A. Das, T. P. Mohammed and M. Sankaralingam, Biological activity of copper porphyrins, *Coord. Chem. Rev.*, 2024, **506**, 215661.

18 S. Mahalingam, M. Durai, C. Sengottaiyan and Y.-H. Ahn, Effective Chemical Vapor Deposition and Characterization of N-Doped Graphene for High Electrochemical Performance, *J. Nanosci. Nanotechnol.*, 2021, **21**, 3183–3191.

19 J. Zhu, X. Guo, H. Wang and W. Song, Cost-effective fabrication and high-frequency response of non-ideal RC application based on 3D porous laser-induced graphene, *J. Mater. Sci.*, 2018, **53**, 12413–12420.

20 H. Tariq, S. U. Awan, D. Hussain, S. Rizwan, S. A. Shah, S. Zainab and M. B. Riaz, Enhancing supercapacitor performance through design optimization of laser-induced graphene and MWCNT coatings for flexible and portable energy storage, *Sci. Rep.*, 2023, **13**, 21116.

21 W. Yang, Y. Liu, Q. Li, J. Wei, X. Li, Y. Zhang and J. Liu, In situ formation of phosphorus-doped porous graphene via laser induction, *RSC Adv.*, 2020, **10**, 23953–23958.

22 Y. Zou, M. Zhong, S. Li, Z. Qing, X. Xing, G. Gong, R. Yan, W. Qin, J. Shen, H. Zhang, Y. Jiang, Z. Wang and C. Zhou, Flexible Wearable Strain Sensors Based on Laser-Induced Graphene for Monitoring Human Physiological Signals, *Polymers*, 2023, **15**, 3553.

23 B. Sindhu, A. Kothuru, P. Sahatiya, S. Goel and S. Nandi, Laser-induced graphene printed wearable flexible antenna-based strain sensor for wireless human motion monitoring, *IEEE Trans. Electron Devices*, 2021, **68**, 3189–3194.

24 M. Sami, M. E. El-Khouly and M. Ghali, Solvent mediated synthesis of multicolor narrow bandwidth emissive carbon quantum dots and their potential in white light emitting diodes, *Sci. Rep.*, 2024, **14**, 24812.

25 M. Skorupska, P. Kamedulski, J. P. Lukaszewicz and A. Ilnicka, The Improvement of Energy Storage Performance by Sucrose-Derived Carbon Foams via Incorporating Nitrogen Atoms, *Nanomaterials*, 2021, **11**, 760.

26 J. Wang, L. Shen, B. Ding, P. Nie, H. Deng, H. Dou and X. Zhang, Fabrication of porous carbon spheres for high-performance electrochemical capacitors, *RSC Adv.*, 2014, **4**, 7538.

27 J. Zheng, S. Zhang, Y. Zeng, X. Li and Q. Zhong, Synergistic effect of oxygen-containing and nitrogen-containing groups on promoting low-temperature denitration over non-metallic carbon-based catalyst, *Mol. Catal.*, 2024, **554**, 113824.

28 C. Maddi, F. Bourquard, V. Barnier, J. Avila, M.-C. Asensio, T. Tite, C. Donnet and F. Garrelie, Nano-Architecture of nitrogen-doped graphene films synthesized from a solid CN source, *Sci. Rep.*, 2018, **8**, 3247.

29 A. Dolgov, D. Lopaev, C. J. Lee, E. Zoethout, V. Medvedev, O. Yakushev and F. Bijkerk, Characterization of carbon contamination under ion and hot atom bombardment in a tin-plasma extreme ultraviolet light source, *Appl. Surf. Sci.*, 2015, **353**, 708–713.

30 N. Hellgren, R. T. Haasch, S. Schmidt, L. Hultman and I. Petrov, Interpretation of X-ray photoelectron spectra of carbon-nitride thin films: new insights from in situ XPS, *Carbon*, 2016, **108**, 242–252.

31 S. R. Kelemen, G. N. George and M. L. Gorbaty, Direct determination and quantification of sulphur forms in heavy petroleum and coals, *Fuel*, 1990, **69**, 939–944.

32 S. Tresintsi, K. Simeonidis, N. Pliatsikas, G. Vourlias, P. Patsalas and M. Mitrakas, The role of SO_4^{2-} surface distribution in arsenic removal by iron oxy-hydroxides, *J. Solid State Chem.*, 2014, **213**, 145–151.

33 N. Mushtaq, G. Chen, L. R. Sidra and X. Fang, Organosoluble and high T_g polyimides from asymmetric diamines containing N-amino and N-aminophenyl naphthalimide moieties, *RSC Adv.*, 2016, **6**, 25302–25310.

34 L. Martins, B. Kulyk, A. Theodosiou, A. Ioannou, C. Moreirinha, K. Kalli, N. Santos, F. Costa, S. O. Pereira and C. Marques, Laser-induced graphene from commercial polyimide coated optical fibers for sensor development, *Opt Laser. Technol.*, 2022, **160**(25), 109047.

35 N. Azam, M. N. Ali and T. J. Khan, Carbon Quantum Dots for Biomedical Applications: Review and Analysis, *Front. Mater.*, 2021, **8**, 700403.

36 S. Bilal, I. A. Mohammed-Dabo, B. B. M. Dewu, O. R. Momoh and S. Abubakar, Refining and Characterisation of Gum Arabic Using Vacuum Filtration Method for Application in Oil and Gas Drilling Fluid Formulation, *J. Exp. Res.*, 2015, **3**, 2315–9650.

37 K.-J. Chuang, C. Jäger, J. C. Santos and T. Henning, Formation of N-bearing complex organic molecules in molecular clouds: ketenimine, acetonitrile, acetaldimine, and vinylamine via the UV photolysis of C_2H_2 ice, *Astron. Astrophys.*, 2024, **687**, A7.

38 J.-U. Lee, C.-W. Lee, S.-C. Cho and B.-S. Shin, Laser-Induced Graphene Heater Pad for De-Icing, *Nanomaterials*, 2021, **11**, 3093.

39 Y. Sun, D. Lee, Y. Wang, S. Li, J. Ying, X. Liu, G. Xu, J. Gwon and Q. Wu, Thermal decomposition behavior of 3D printing filaments made of wood-filled polylactic acid/starch blend, *J. Appl. Polym. Sci.*, 2020, **138**, 49944.

40 G. Jiang, D. Wang, H. Du, X. Wu, Y. Zhang, Y. Tan, L. Wu, J. Liu and X. Zhang, Reduced Coefficients of Linear Thermal Expansion of Colorless and Transparent Semi-Alicyclic Polyimide Films via Incorporation of Rigid-Rod Amide Moiety: Preparation and Properties, *Polymers*, 2020, **12**, 413.

41 S. M. Tareq, N. A. AbdulWahhab and A. H. Al-araji, Effect of Violet Laser Irradiation on the Optical Properties of Polyvinyl Alcohol/Methyl Orange Composite Thick Films: A Model for Medical Applications, *Eng. Proc.*, 2023, **59**, 236.

42 D. Larowska, A. Wojcik, M. Mazurkiewicz-Pawlicka, A. Malolepszy, L. Stobiński, B. Marciniak and A. Lewandowska-Andralojc, Cationic Porphyrin-Graphene Oxide Hybrid: Donor-Acceptor Composite for Efficient Photoinduced Electron Transfer, *ChemPhysChem*, 2019, **20**, 1054–1066.

43 M. de J. Nava-Ramírez, A. Vázquez-Durán, J. de D. Figueroa-Cárdenas, D. Hernández-Patlán, B. Solís-Cruz, G. Téllez-Isaías, C. López-Coello and A. Méndez-Albores, Removal of

Aflatoxin B1 Using Alfalfa Leaves as an Adsorbent Material: A Comparison between Two In Vitro Experimental Models, *Toxins*, 2023, **15**, 604.

44 M. Kim, S. Hwang and J.-S. Yu, Novel ordered nanoporous graphitic C_3N_4 as a support for Pt–Ru anode catalyst in direct methanol fuel cell, *J. Mater. Chem.*, 2007, **17**, 1656–1659.

45 A. B. D. Nandiyanto, R. Ragadhita and M. Fiandini, Interpretation of Fourier Transform Infrared Spectra (FTIR): A Practical Approach in the Polymer/Plastic Thermal Decomposition, *Indones. J. Sci. Technol.*, 2023, **8**, 113–126.

46 A. Orlando, F. Franceschini, C. Muscas, S. Pidkova, M. Bartoli, M. Rovere and A. Tagliaferro, A Comprehensive Review on Raman Spectroscopy Applications, *Chemosensors*, 2021, **9**, 262.

47 K. Aljakouch, T. Lechtonen, H. K. Yosef, M. K. Hammoud, W. Alsaidi, C. Kötting, C. Mügge, R. Kourist, S. F. El-Mashtoly and K. Gerwert, Raman Microspectroscopic Evidence for the Metabolism of a Tyrosine Kinase Inhibitor, Neratinib, in Cancer Cells, *Angew. Chem., Int. Ed.*, 2018, **57**, 7250–7254.

48 S. F. El-Mashtoly and K. Gerwert, Diagnostics and Therapy Assessment Using Label-Free Raman Imaging, *Anal. Chem.*, 2022, **94**, 120–142.

49 S. Venkatachalam, D. Bertin, G. Ducournau, J. F. Lampin and D. Hourlier, Kapton-derived carbon as efficient terahertz absorbers, *Carbon*, 2016, **100**, 158–164.

50 K. G. Mikheev, R. G. Zonov, D. L. Bulatov, A. E. Fateev and G. M. Mikheev, Laser-Induced Graphene on a Polyimide Film: Observation of the Photon Drag Effect, *Tech. Phys. Lett.*, 2020, **46**, 458–461.

51 Y. Lee, M. J. Low, D. Yang, H. K. Nam, T.-S. D. Le, S. E. Lee, H. Han, S. Kim, Q. H. Vu, H. Yoo, H. Yoon, J. Lee, S. Sandeep, K. Lee, S.-W. Kim and Y.-J. Kim, Ultra-thin light-weight laser-induced-graphene (LIG) diffractive optics, *Light: Sci. Appl.*, 2023, **12**, 146.

52 K.-I. Sasaki, Basic Principles of Raman Spectroscopy for Graphene, *NTT Tech. Rev.*, 2013, **11**, 10–14.

53 L. M. Malard, M. A. Pimenta, G. Dresselhaus and M. S. Dresselhaus, Raman spectroscopy in graphene, *Phys. Rep.*, 2009, **473**, 51–87.

54 A. C. Ferrari, J. C. Meyer, V. Scardaci, C. Casiraghi, M. Lazzeri, F. Mauri, S. Piscanec, D. Jiang, K. S. Novoselov, S. Roth and A. K. Geim, Raman Spectrum of Graphene and Graphene Layers, *Phys. Rev. Lett.*, 2006, **97**, 187401.

55 Y. Hao, Y. Wang, L. Wang, Z. Ni, Z. Wang, R. Wang, C. K. Koo, Z. Shen and J. T. L. Thong, Probing Layer Number and Stacking Order of Few-Layer Graphene by Raman Spectroscopy, *Small*, 2010, **6**, 195–200.

56 B. Chakraborty, A. Bera, D. V. S. Muthu, S. Bhowmick, U. V. Waghmare and A. K. Sood, Symmetry-dependent phonon renormalization in monolayer MoS_2 transistor, *Phys. Rev. B: Condens. Matter Mater. Phys.*, 2012, **85**, 161403.

57 A. Das, S. Pisana, B. Chakraborty, S. Piscanec, S. K. Saha, U. V. Waghmare, K. S. Novoselov, H. R. Krishnamurthy, A. K. Geim, A. C. Ferrari and A. K. Sood, Monitoring dopants by Raman scattering in an electrochemically top-gated graphene transistor, *Nat. Nanotechnol.*, 2008, **3**, 210–215.

58 S. Chen, Q. Li, Q. Zhang, Y. Qu, H. Ji, R. S. Ruoff and W. Cai, Thermal conductivity measurements of suspended graphene with and without wrinkles by micro-Raman mapping, *Nanotechnology*, 2012, **23**, 365701.

59 N. El-Shafai, M. E. El-Khouly, M. El-Kemary, M. S. Ramadan and M. S. Masoud, Self-assembly of porphyrin on graphene oxide in aqueous medium: fabrication, characterization, and photocatalytic studies, *Photochem. Photobiol. Sci.*, 2019, **18**, 2071–2079.

60 G. V. Fuentes, E. N. Doucet, A. Abraham, N. K. Rodgers, F. Alonso, N. Euceda, M. H. Quinones, P. A. Riascos, K. Pierre, N. H. Sarker, M. Dhar-Mascareno, M. Cotlet, K. Kisslinger, F. Camino, M. Li, F. Lu and R. Gao, Nanocomposite liposomes for pH-controlled porphyrin release into human prostate cancer cells, *RSC Adv.*, 2020, **10**, 17094–17100.